Development of Miniature Bearingless Motors for RVAD and Fontan Circulation Assist Devices

Takahiro NOGUCHI*, Pranava SINHA**, William A. SMITH*** and Eric L. SEVERSON*
* Department of Mechanical Engineering, University of Minnesota
111 Church St SE, Minneapolis, Minnesota, USA
E-mail: tnoguchi@umn.edu
** Department of Pediatric Cardiac Surgery, University of Minnesota
420 Delaware Street SE, Minneapolis, Minnesota, USA
*** Perfusion Solution Inc.
4320 Mayfield Rd, Cleveland, Ohio, USA

Abstract
This paper presents the development of a miniature bearingless motor for pediatric blood pump applications. Three bearingless machine topologies are investigated: the traditional bearingless homopolar motor (BHPM), the bearingless consequent-pole motor (BCPM), and the hybrid version of these two (BHCPM). A multi-objective optimization framework is implemented to minimize the stack length while achieving required torque and force performance. To enable rapid and accurate evaluation of these machines, a novel evaluation algorithm is developed for the optimization study that utilizes parallel 3D finite element analysis (FEA) solves. The results show that the BHCPM is able to meet the proposed blood pump requirements with an axial length that is up to 60% shorter than the BHPM. The role of the field coil magnetomotive force (MMF) is examined and it is found that adding homopolar flux to create a BHCPM can further reduce the stack length, but tends to increase torque ripple and force vector error, highlighting a critical trade-off in the design of compact and stable bearingless machines.

Keywords : Bearingless homopolar motors, Consequent-pole motors, Blood pump, Multi-objective optimization.

1. Introduction

This paper focuses on the development of a bearingless motor for use in a blood pump designed for two patient groups: 1) Fontan patients who lack a functioning right ventricle and 2) patients whose right ventricle has experienced significant functional failure. In patient group 1, the right ventricle is either absent, small, or does not function properly due to congenital heart disease, necessitating Fontan surgery. This patient group consists of children and young adults and is expected to benefit from an assist device that compensates for the loss of right ventricular function. In North America, the Fontan patient treatment market is approximately 500 to 1,000 surgical procedures per year, Cleveland et al. (2024).

Adult patients presenting with heart failure predominantly suffer from left heart failure and are often treated with left ventricle assist devices (LVADs). However, 20% of these patients need support for a failing right heart. These patients comprise the second group that will benefit from this paper's proposed pump. The market for right ventricular assist devices (RVADs) is one-fifth that of LVADs in North America, which is approximately 2,500 to 3,000 surgical procedures per year, Adamopoulos et al. (2024). Use of commercial LVADs as RVADs poses significant problems as LVADs are designed for systemic circulation and require a blood pressure of 100-135 mmHg, while RVADs are designed for pulmonary circulation and require lower blood pressure (typically 20-30 mmHg). As the hemodynamic requirements for Fontan Support and RVAD pumps are similar, there is a unique opportunity to develop a pump with wider commercial application that would serve both a niche market (failing Fontan circulation) and the larger RVAD market.

Bearingless motors eliminate the need for mechanical bearings by utilizing magnetic forces to suspend the rotor shaft. To design bearingless motors for blood pump applications, several medical aspects must be carefully considered, such as minimizing shear stress, ensuring well-washed blood flow paths, and avoiding blood cell damage and thrombus formation. Examples of bearingless blood pumps include the radial flow HeartMate III, which has been commercialized as an LVAD,

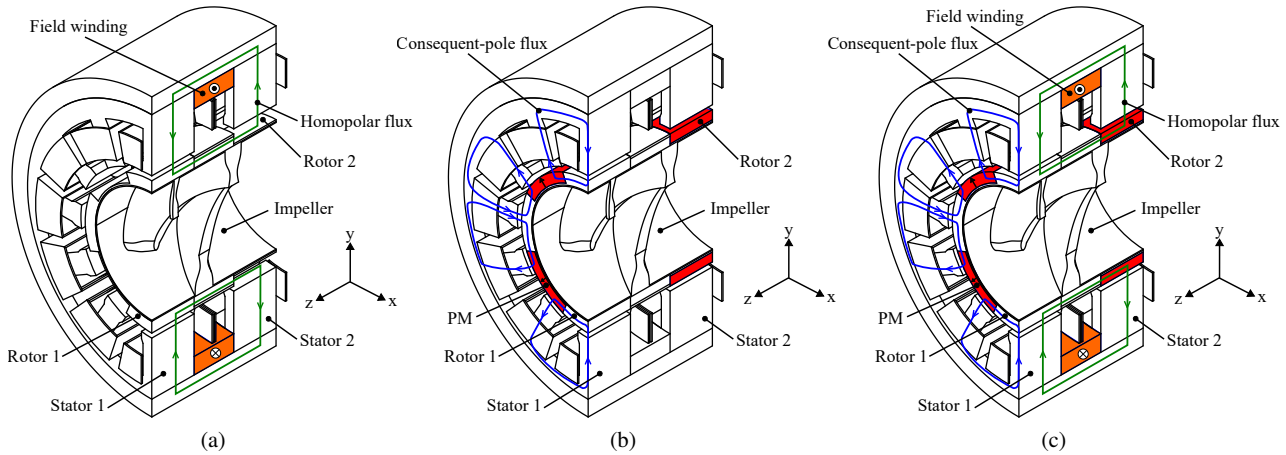

Fig. 1: Cross section drawing: (a) BHPM, (b) BCPM, and (c) BHCPM.

Bourque et al. (2001). A centrifugal type bearingless motor was proposed for a total artificial heart that integrates both left and right heart functions in Kurita et al. (2018). Bearingless AC homopolar motor (BHPM) configurations have been developed in He et al. (2023); Gruber et al. (2014) for blood pumps.

For the aims of this paper, compact motor size is especially critical to accommodate smaller anatomical structures, particularly in pediatric patients, and to fit within the tight space constraints of previous complex surgical repairs in patients with Fontan failure. Bearingless motors of the $p_s = 1$ pole-pair category, like the BHPM, offer a key advantage for miniaturization by eliminating the need for rotary position sensors for levitation control. However, the BHPM is notoriously challenging to design due to its 3D flux paths requiring computationally-intensive 3D finite element analysis (FEA). Due to this, design optimizations are typically limited to a small number of case studies He et al. (2023).

The primary contribution of this paper is to investigate the integration and miniaturization of $p_s = 1$ bearingless machines with a blood pump to a size suitable for implantation in a child. This paper studies all three types of $p_s = 1$ machines: 1) BHPM, 2) bearingless consequent-pole motor (BCPM), and 3) their hybrid configuration, referred to as the BHCPM. A secondary contribution is the development of a modeling approach to rapidly evaluate $p_s = 1$ bearingless motors in a multi-objective optimization. The paper presents optimization results characterizing the design space for maximum miniaturization. This optimization study shows that the BHCPM can be designed to be 60% more compact than the BHPM machine, while the BHPM consistently achieves the lowest force vector error angle ($\leq 5°$).

2. Design of proposed blood pump

The design concept for the proposed blood pump is now presented along with the design requirements.

2.1. Integration of blood pump with the bearingless motor

The cross-sectional drawing of the proposed pump is shown in Figure 1. The pump features a hollow shaft that is configured with two rotor segments (to enable 4-DOF control) and integrated with an axial-flow impeller. The impeller is designed so that if the rotor stops rotating, the blood can still travel through the center. The paper considers the pump to be integrated with the following three different bearingless motor structures:

1) BHPM, Fig. 1a, where a field coil is integrated between the two stators to create a homopolar flux;
2) BCPM, Fig. 1b, where PMs are embedded within the rotor and magnetized in the same direction; and
3) BHCPM, Fig. 1c, which is a hybrid of the BHPM and BCPM machines and has both a field coil and rotor magnets.

Note that all three machines avoid the need for an encoder to detect angular position.

2.2. Bearingless motor design requirements

This subsection outlines the size requirements of the proposed blood pump, considering medical constraints to avoid adverse patient effects. Figures 2a and 2b label the machine's dimension parametrization along with materials, with the stator outer radius r_{so} and total axial length l_{sl} each limited to 20 mm to ensure that resulting pump can fit within pediatric patients.

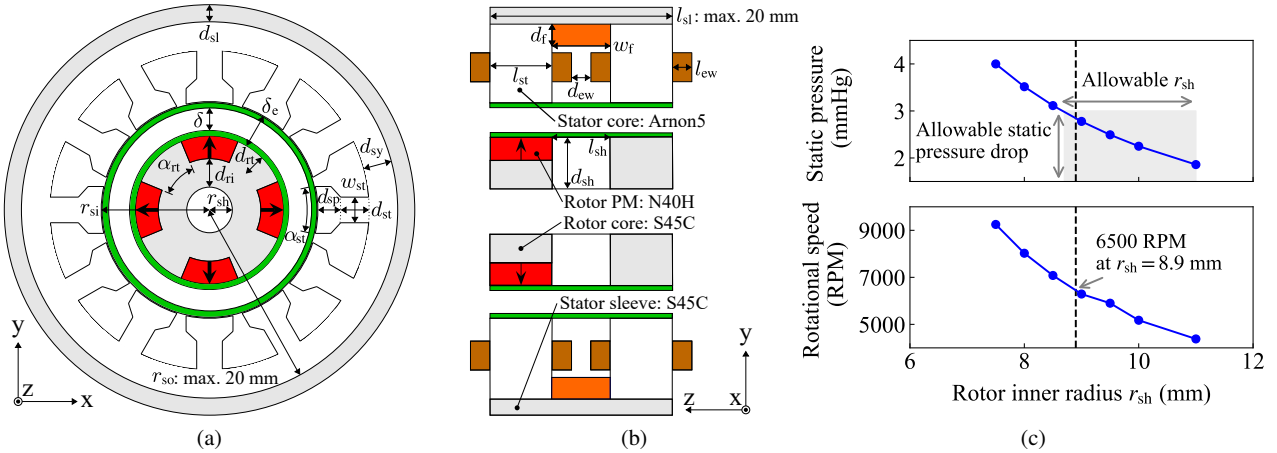

Fig. 2: Design parameters and requirements for the proposed blood pump: (a) xy cross section, (b) yz cross section, and (c) static pressure drop analysis and required rotational speed with respect to rotor inner radius.

A key advantage of this design is that even if the pump stops operating, the blood flow path remains direct and minimally obstructed to reduce risks to patient survival. To obtain this goal, a prototype of the proposed pump was fabricated and tested. Figure 2c presents scaled test data to show the relationship between static pressure drop and rotor inner radius r_{sh} when the rotor is not spinning. This represents the pump failure condition, where r_{sh} needs to be sized so that the static pressure drop is ≤ 3 mmHg (to minimize circulatory burden). While larger r_{sh} values lead to lower pressure, $r_{sh} = 8.9$mm is selected to reserve sufficient space for the bearingless motor (considering the $r_{so} < 20$mm requirement).

The rotational speed of the pump is determined from additional scaled pump test data, shown in the bottom plot of Fig. 2c, as 6500 RPM to ensure a flow rate of 10 L/min at 30 mmHg. This requires the bearingless motor to have a torque rating of 12 mNm. A force rating of 0.8N is determined based on gravitational loading of the rotor and blood mass with a safety factor of 3. These parameters are listed Table 1 and used in the optimization study of Section 3.

Table 1: Fixed design parameters.

Parameter (Unit)	Symbol	Value
Rated torque (mNm)	τ^*	12
Rated force (N)	F^*	0.8
Rated current density (A_{rms}/mm^2)	J	5
Stator inner radius (mm)	r_{si}	12.5
Stator outer radius (mm)	r_{so}	20
Stator pole thickness (mm)	d_{sp}	1.05

Table 2: Free variables and their ranges.

Parameter (Unit)	Symbol	Value
Stator tooth face angle (deg)	α_{st}	[20, 28]
Stator tooth width (mm)	w_{st}	[2, 5]
Rotor tooth height (mm)	d_{rt}	[1, 2.5]
Rotor core angular span (deg)	α_{rt}	[40, 45]
Stator sleeve thickness (mm)	d_{sl}	[1, 3]
Field coil MMF[a] (AT)	$N_f i_f$	[500, 1500]

Table 3: Dependent variables.

Parameter (Unit)	Symbol	Value
Stator tooth depth (mm)	d_{st}	$r_{so} - d_{sy} - d_{sp} - r_{si}$
Stator yoke thickness (mm)	d_{sy}	d_{ri}
PM angular span (deg)	α_m	$90 - \alpha_{rt}$
Rotor back iron thickness (mm)	d_{ri}	$r_{si} - \delta - d_m - r_{sh}$
PM thickness (mm)	d_m	d_{rt}
Outer rotor radius (mm)	r_{ro}	$r_{si} - \delta$
Length of end windings (mm)	l_{ew}	$0.25\pi(r_{si} + d_{sp} + 0.5d_{st})/6$ $+0.25w_{st}$
Field coil width (mm)	w_f	$2l_{ew} + d_{ew}$
Field coil height (mm)	d_f	$0.9d_{sy}$
Shaft thickness (mm)	d_{sh}	$d_{ri} + d_{rt}$
Shaft length (mm)	l_{sh}	$2l_{ew} + d_{ew}$

[a]The free variable, field coil MMF $N_f i_f$, is only applicable to the BHPM and BHCPM machines. For the BCPM machine, this value is set to zero during optimization.

3. Optimization framework for BHPM, BCPM, and BHCPM

This section proposes a modeling framework uniquely suited to explore the design space of the BHPM, BCPM, and BHCPM machines illustrated in Fig 1. This study aims to minimize the axial length of the machine having acceptable torque and force ripple. A key technique introduced in this study is a novel evaluation methodology that enables rapid performance estimation of the BHPM, BCPM, and BCHPM. To achieve this, 3D FEA is performed at a limited number of rotor positions that can be evaluated in parallel, instead of simulating the full rotational range. This approach significantly reduces computational effort while satisfying the target specifications.

3.1. Problem formulation

This study investigates the bearingless machine configuration of 12 stator slots, 4 pole-pair rotor, and a 1 pole-pair suspension field, using a double-layer concentrated winding topology designed as a combined winding, see Khamitov and Severson (2023). Table 2 lists free variables along with their ranges explored during optimization. Table 3 presents the dependent variables determined by the fixed parameters and free variables.

Similar to Chen et al. (2021), the optimization is performed using the Multi-Objective Evolutionary Algorithm based on Decomposition (MOEA/D), Zhang and Li (2007). The algorithm searches the free variables listed in Table 2 to minimize the objectives of Eq. (1). These objectives have been selected for the miniaturized blood pump application as 1) stack length l_{st}, 2) torque ripple τ_{rip}, 3) force vector magnitude error E_{m}, and 4) force vector error angle E_{a}.

$$O_1 = l_{\mathrm{st}}, \quad O_2 = \tau_{\mathrm{rip}} = \frac{\max(|\tau(\theta) - \tau_{\mathrm{avg}}|)}{\tau_{\mathrm{avg}}}, \quad O_3 = E_{\mathrm{m}} = \frac{\max(|F(\theta) - F_{\mathrm{avg}}|)}{F_{\mathrm{avg}}}, \quad O_4 = E_{\mathrm{a}} = \max(|\phi(\theta) - \phi_{\mathrm{avg}}|) \tag{1}$$

Here, τ_{avg} and F_{avg} are the average of torque $\tau(\theta)$ and force $F(\theta) = \sqrt{F_{\mathrm{x}}^2(\theta) + F_{\mathrm{y}}^2(\theta)}$ with respect to the rotor angle θ. The torque/force values represent the total shaft torque/forces (the sum of both rotor units). The force vector error angle E_{a} quantifies angular deviation between the instantaneous angle of the force vector $\phi(\theta) = \mathrm{atan2}(F_{\mathrm{y}}(\theta), F_{\mathrm{x}}(\theta))$ and the average angle of the force vector ϕ_{avg}, which has to be minimized to stabilize the levitation control.

3.2. Design flow with the proposed evaluation methodology

This subsection presents the proposed optimization design flow to rapidly evaluate the bearingless machines using 3D FEA. Figure 3 provides a flowchart of the optimization, include the novel evaluation method. In Fig. 3, the optimization process begins by generating a set of free variables through the algorithm. These variables are then subjected to two FEA evaluations to 1) determine the required stack length and stator currents (see Subsection 3.2.2) and 2) determine torque ripple and force vector error (see Subsection 3.2.3). The basic idea is to formulate the design evaluation as a set of static FEA solves, each examining machine performance at a distinct rotor angle. Since each static FEA solve is indendent of all other solves, this approach enables the use of parallel computation, in contrast to full-transient FEA which has less benefit from parallelization. To achieve this, it is necessary to determine both the appropriate maximum allowable rotor rotation between FEA solves (referred to as "simulation step") and the minimum rotational range of the rotor required to capture the torque/force ripple.

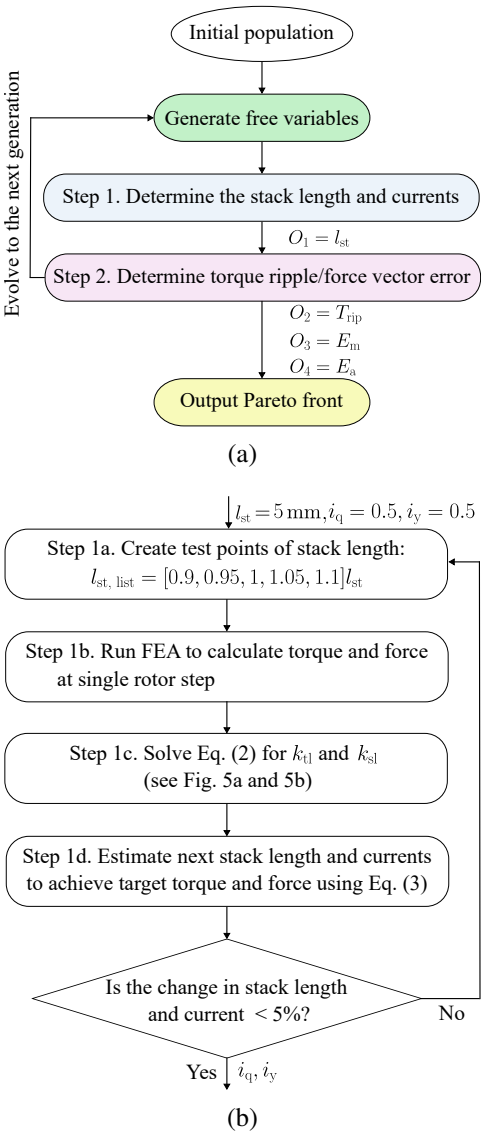

Fig. 3: Optimization: (a) overview, and (b) detailed description of Step 1.

3.2.1. Preliminary analysis of force and torque waveforms

The force and torque waveforms of three designs randomly generated by the optimization algorithm are now studied to determine parameters necessary for the proposed design evaluation algorithm. The results are shown in Figs. 4a and 4b, where it is observed that all designs exhibit similar patterns of torque and force with respect to the rotor angle θ.

First, it is noted that the average values of force and and torque can be estimated by evaluating the designs at a rotor angle of $\theta = 13°$.

Second, the appropriate simulation step and rotational range required to accurately capture the torque and force ripple performance are considered. Figures 4c and 4d show the harmonic spectra of the force and torque. The highest significant harmonic is order 24 (torque ripple), while the lowest significant harmonic is 8th (force ripple). The minimum rotational range of the rotor required to capture the torque/force ripple is set to 45°(= 360/8) based on the lowest harmonic (8th, from force waveform). The simulation step is determined by the highest harmonic (24th, from torque waveform), which has a period of 15°(= 360/24). Based on the number of CPU cores available in the authors' simulation server, a step of 4° is selected.

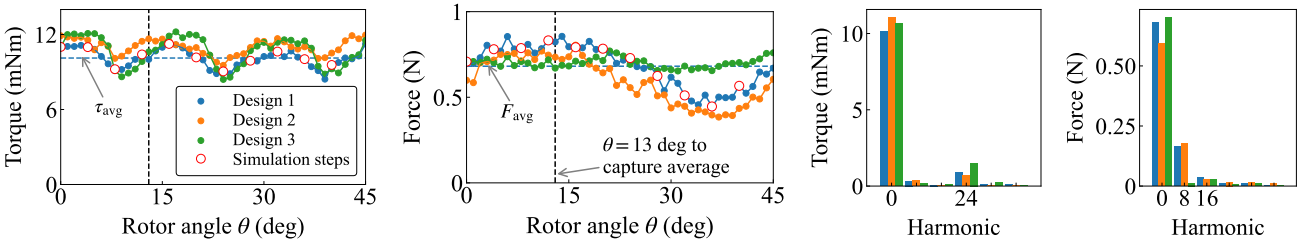

Fig. 4: Preliminary analysis results to determine simulation step and total rotational range: (a) torque with respect to rotor angles, (b) force with respect to rotor angles, (c) FFT result of torque, and (d) FFT result of force waveform.

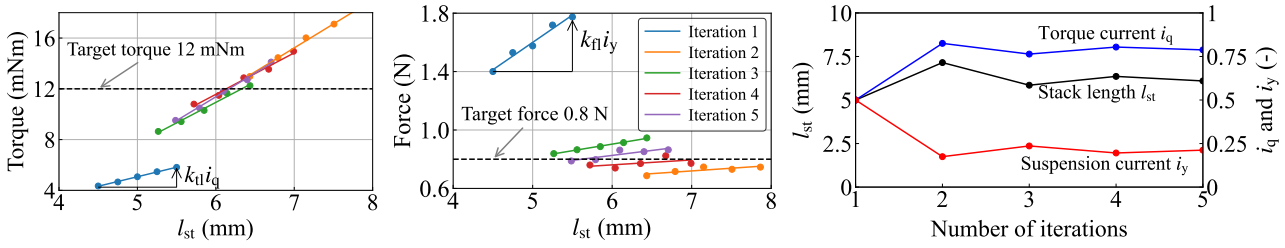

Fig. 5: Iteration process to determine the stack length and currents: (a), (b) torque and force with respect to the stack length, and (c) iterations of stack length and torque/force currents.

3.2.2. Algorithm step 1: determine the stack length and currents

This subsection provides a detailed explanation of Step 1 from Fig. 3. In radial flux motors, rated torque and force can be achieved by scaling the stack length of a design. However, this is not the case for the homopolar machines due to the 3D nature of the homopolar field. This novel algorithm uses a set of parallel 3D FEA solves to rapidly determine the combination of stack length l_{st} and torque i_q and suspension i_y currents that produce the desired torque and force. The stator coils are assumed to carry rated current and i_q and i_y represent the fraction of that current dedicated to force vs torque, meaning that $i_q + i_y = 1$. The algorithm of Fig. 3b starts by assuming $l_{st} = 5$ mm, $i_q = 0.5$, and $i_y = 0.5$.

In Step 1a, a list of stack lengths is generated in increments of ±5%.

In Step 1b, a 3D FEA simulation is performed at $\theta = 13°$ (the rotor angle determined in Section 3.2.1) to estimate the average torque and force for each stack length. After running the single-step FEA, two plots of torque and force with respect to the stack length can be obtained as shown in Figs. 5a and 5b. From these plots, both torque and force show nearly linear behavior due to their narrow range of stack length, i.e., ±0.5 mm.

In Step 1c, the torque and force per ampere per stack length, k_{tl} and k_{fl}, are calculated. These coefficients correspond to the slopes in Figs. 5a and 5b, when torque and force are proportional to the stack length and currents:

$$\tau = k_{tl} i_q l_{st}, \quad F = k_{fl} i_y l_{st} \tag{2}$$

In Step 1d, the algorithm estimates the stack length and torque/suspension currents for the next iteration required to achieve the target torque and force. To obtain these values, the following relationships are derived by solving Eq. (2) for l_{st}, i_q, and i_y under the constraint that $i_q + i_y = 1$:

$$l_{st}^{k+1} = \frac{\tau^*}{k_{tl}^k} + \frac{F^*}{k_{fl}^k}, \quad i_q^{k+1} = \frac{\tau^*}{k_{tl}^k l_{st}^{k+1}}, \quad i_y^{k+1} = \frac{F^*}{k_{fl}^k l_{st}^{k+1}} \tag{3}$$

Here, τ^* and F^* are desired target torque and force. Note that the superscript k denotes the k-th iteration in this scaling process. Each value with the superscript $k+1$ represents the scaled parameters used in the next iteration. In principle, the stack length and current values should be uniquely determined. However, due to the nonlinearities of the homopolar machines, the scaling procedure is repeated iteratively until the errors between consecutive loops fall below 5%. Figure 5c demonstrates this process, which converges within five iterations in this case. In this example, the final values obtained are stack length $l_{st} = 6.09$ mm, torque current $i_q = 0.79$, and suspension current $i_y = 0.21$.

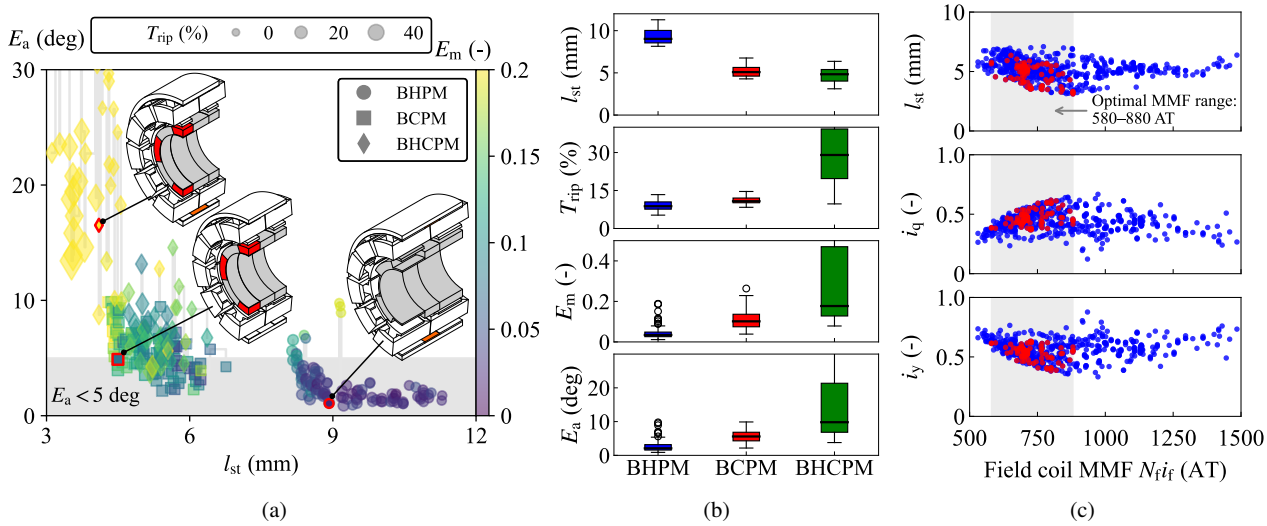

(a) (b) (c)

Fig. 6: Results of optimization for BHPM, BCPM, and BHCPM: (a) Pareto fronts. The gray-shaded regions indicate the preferred range of $E_a < 5$ deg, (b) box and whisker plots , (c) trends of l_{st}, i_q, and i_y to $N_f i_f$.

3.2.3. Algorithm step 2: determine torque ripple and force vector error

To calculate the optimization objectives $O_2 = \tau_{rip}$, $O_3 = E_m$, and $O_4 = E_a$, the ripple components in torque and force are evaluated in Step 2 of Fig. 3a. Using the finalized stack length and current values from the initial evaluation step, the design is simulated at 11 rotor angles (see red markers in Figs. 4a and 4b), as discussed in Subsection 3.2.1.

4. Optimization results and design space

This section presents results of the design space exploration of the BHPM, BCPM, and BHCPM machines. The Pareto front is shown and general design trends between the four objective variables are discussed.

4.1. Optimization results

Figure 6a shows the final Pareto fronts obtained by this optimization study. The BHPMs (circle markers) exhibit the lowest torque/force ripple, while requiring a significantly longer stack length. In contrast, the BHCPMs (diamond markers) have the shortest stack length, but tend to have higher torque/force ripple. The BCPMs (square markers) have intermediate characteristics between BHPM and BHCPM machines, with reasonably small stack length and ripple components. These trends indicate that combining the field coil MMF and rotor PMs reduces the stack length (i.e., improve torque/force density) at the expense of increased torque ripple and force vector error.

Figure 6b illustrates box and whisker plots of the four objective variables for all designs on the Pareto front. From Fig. 6b, the minimum stack length of 8.14 mm can be seen for the BHPM machine, while the BHCPM can achieve 3.19 mm stack length. This indicate that the BHCPM can potentially reduce the axial length by 60% over the BHPM machine. For the force vector error angle, the interquartile range remains within 5 degrees for the BHPM machine. Although this highlights that stable force generation is possible with the BHPM design, it tends to require a larger stack length in this case, indicating a trade-off between stack length and ripple components. It was eventually found that BHPMs are unable to satisfy the axial length constraint $l_{sl} < 20$ mm, discussed in Section 2.2, when end windings l_{ew} and clearance between the stator coils d_{ew} are added to the stack length l_{st} (see Fig. 2b).

Figure 6c illustrates the trend of l_{st}, i_q, and i_y with respect to the field coil MMF in the BHCPM design. The blue markers represent all archived designs (approximately 700), while red markers represent the designs from the Pareto front. It can be observed that the optimal MMF values that minimize the stack length are within range of 580 to 880 AT. The mechanism behind this trend will be investigated in detail in Subsection 4.3.

4.2. Selected designs

Table 4 lists machine dimensions (focusing on free variables) and performance of three selected designs. These designs were selected from Fig. 6a (indicated by red markers) to highlight the strengths of each topology. For the BHPM, the selected design prioritizes small force vector error angle; the BHCPM design is selected with small stack length, albeit large force vector error angle; the BCPM design is selected as a compromise between stack length and force vector error angle.

Table 4: Machine dimensions and performance of selected designs.

Parameter (Unit)	Symbol	BHPM	BCPM	BHCPM
Stator tooth face angle (deg)	α_{st}	27.63	27.52	27.24
Stator tooth width (mm)	w_{st}	2.926	2.649	3.419
Rotor tooth height (mm)	d_{rt}	2.069	2.392	2.338
Rotor core angular span (deg)	α_{rt}	44.86	44.60	43.81
Stator sleeve thickness (mm)	d_{sl}	1.401	1.282	1.541
Field coil MMF (AT)	$N_f I_f$	782.9	0	714.0
Stack length (mm)	l_{st}	8.920	4.496	4.097
Torque ripple (%)	τ_{rip}	4.844	12.58	6.152
Force vector magnitude error (-)	E_m	0.021	0.075	0.216
Force vector error angle (deg)	E_a	1.061	4.885	16.51

4.3. Required field coil MMF to minimize the stack length

In Subsection 4.1, the optimization study demonstrated that the BHCPM can potentially reduce the axial length compared to the BHPM machine. This subsection now investigates the fundamental mechanism behind this advantage, using the selected BHCPM machine from Subsection 4.2 as a representative design. Figure 7a shows the trends of τ, F_y, τ_{rip}, and E_a when varying the field coil MMF. Notice that $N_f i_f = 0$ AT corresponds to the case of a pure BCPM configuration. As $N_f i_f$ increases, the torque increases and reaches its peak value at $N_f i_f = 714$ AT, and decreases subsequently. On the other hand, the force exhibits a "positive" peak at $N_f i_f = -450$ AT, and becomes negative after $N_f i_f = 300$ AT, i.e., the force is now generated in the opposite direction. The force reaches its "negative" peak at $N_f i_f = 750$ AT, which occurs near the maximum torque condition. This notably indicates that the MMF can potentially enhance both torque and force capability in comparison to BCPM, while the direction of the force reverses above a certain field coil MMF.

Figure 7b shows the magnetic flux density waveforms and their FFT in the airgap of stator 1 side under $N_f i_f = -450$, 0, and 714 AT. It is observed that increasing the field coil MMF enhances the 4 pole-pair component, thereby increasing torque generation. This explains why increasing the field coil MMF in the positive direction leads to increasing torque. In contrast, the DC (homopolar) component, which contributes to force creation, decreases as MMF increases. Notice that when the MMF is negative value of $N_f i_f = -450$ AT, the homopolar component is positive value of 0.42 T, whereas when the MMF is a positive value of $N_f i_f = 714$ AT, the homopolar component becomes negative value of -0.12 T (see flux waveform of Fig. 7b). This explains why the sign of the generated forces reverses depending on the sign of the applied MMF. It is interesting to note that even with no homopolar field coil excitation, the consequent-pole rotor magnets are resulting in a hompolar field because of the magnetic stator sleeve and rotor core / pump material (S45C), see Fig. 2b.

The proposed algorithm (see Fig. 3b) is now reapplied to the selected BHCPM design to explore the effect of varying the field coil MMF from -1500 to 1500 AT, while the target torque and force specifications are satisfied. Figure 7c presents the results of this analysis. Interestingly, although the stack length generally decreases with increasing MMF, the minimum value is not necessarily achieved at the maximum MMF. Instead, an optimal MMF of approximately 750 AT is identified to obtain the minimum stack length. This trend is consistent with the findings in Fig. 6c, where the overall optimization converges to the MMF range of 550 to 880 AT in this machine design. Note that Fig. 7c has gray-shaded regions where k_{tl} and/or k_{fl} become so low that no stack length / current combination exist that can meet the force and torque specification (e.g., see Fig. 7a, torque at $N_f i_f = -1500$ AT or force at $N_f i_f = 300$ AT).

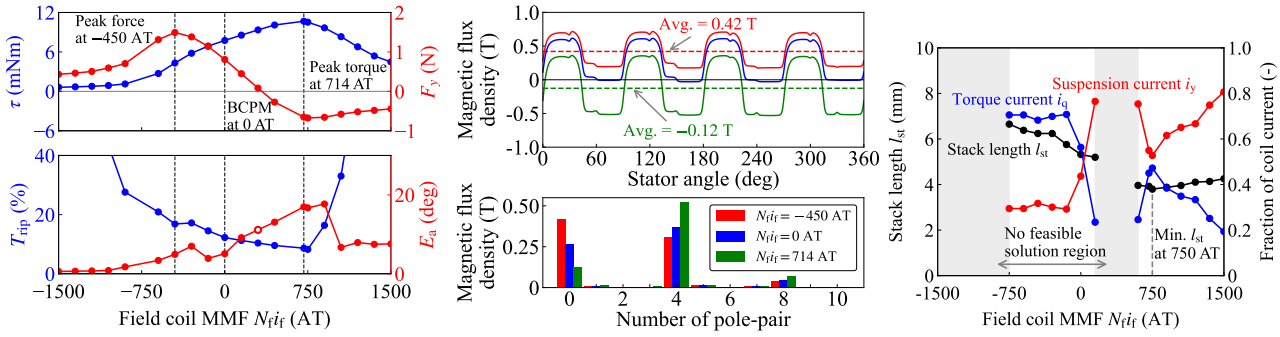

(a) (b) (c)

Fig. 7: Analysis results of BHCPM machine: (a) machine performance versus MMF, (b) flux density distribution of airgap and FFT results, and (c) trends of stack length and torque/force current with respect to the MMF.

In summary, these finding suggests that the magnitude and polarity of the field coil MMF are essential aspects of the machine design for BHCPMs, which affect torque and force generation. This finding is further supported by the optimization results, which reveals a necessary trade-off between torque/force performance and ripple components, while ensuring to minimize the axial length.

5. Conclusion

This study investigated the miniaturization of BHPM, BCPM, and BHCPM bearingless machines for blood pump applications. A novel design evaluation method was developed and linked to an optimization algorithm to reduce the axial length while minimizing torque and force ripple metrics. The paper finds that the BHCPM is capable of the greatest miniaturization (shortest stack length, as low as 3.19 mm), but with a large force vector error angle that compromises the ability to stably levitated. In contrast, the BHPM has the lowest force vector error angle (1.06 degrees), indicating superior levitation stability, but was too large to satisfy the axial length requirement. The BCPM was found to be capable of meeting the design sizing requirements with acceptable force vector error for high performance levitation. To understand the trade-offs of the hybrid BHCPM structure, the paper investigated the field coil MMF required to minimize the stack length and finds that there is an optimal range of MMF (580-880 AT for this topology) that results in greatest miniaturization.

Ultimately, the paper concludes that the BHCPM is most promising for miniature blood pumps due to its combination of small form factor and precise force and torque capability. However, since the BHCPM is shown to have the greatest miniaturization potential, future efforts are recommended to attempt to mitigate force and torque ripple in this machine, such as alternate winding design and more advanced stator tooth tip shapes.

6. Acknowledgments

FEA tools used in this work were provided by the JSOL Corporation (JMAG).

References

Adamopoulos, S., Bonios, M., Ben Gal, T., Gustafsson, F., Abdelhamid, M., Adamo, M., Bayes-Genis, A., Böhm, M., Chioncel, O., Cohen-Solal, A., et al. (2024). Right heart failure with left ventricular assist devices: Preoperative, perioperative and postoperative management strategies. A clinical consensus statement of the Heart Failure Association (HFA) of the ESC. *European Journal of Heart Failure*, 26(11):2304–2322.

Bourque, K., Gernes, D. B., Loree, H. M., Richardson, J. S., Poirier, V. L., Barletta, N., Fleischli, A., Foiera, G., Gempp, T. M., Schoeb, R., et al. (2001). HeartMate III: pump design for a centrifugal LVAD with a magnetically levitated rotor. *ASAIO journal*, 47(4):401–405.

Chen, J., Fujii, Y., Johnson, M. W., Farhan, A., and Severson, E. L. (2021). Optimal design of the bearingless induction motor. *IEEE Transactions on Industry Applications*, 57(2):1375–1388.

Cleveland, V., Contento, J., Mass, P., Hardikar, P., Wu, Q., Liu, X., Aslan, S., Loke, Y.-H., Krieger, A., Lunos, S., et al. (2024). In vitro investigation of axial mechanical support devices implanted in the novel convergent cavopulmonary connection fontan. *European Journal of Cardio-Thoracic Surgery*, 65(1).

Gruber, W., Rothböck, M., and Schöb, R. T. (2014). Design of a novel homopolar bearingless slice motor with reluctance rotor. *IEEE Transactions on Industry Applications*, 51(2):1456–1464.

He, Z., Sugita, N., and Shinshi, T. (2023). A novel heteropolar bearingless slice motor with a pm-free rotor for centrifugal blood pump applications. *IEEE Access*, 11:100114–100124.

Khamitov, A. and Severson, E. L. (2023). Design of multi-phase combined windings for bearingless machines. *IEEE Transactions on Industry Applications*, 59(3):3243–3255.

Kurita, N., Ishikawa, T., Saito, N., Masuzawa, T., and Timms, D. L. (2018). A double-sided stator type axial bearingless motor development for total artificial heart. *IEEE Transactions on Industry Applications*, 55(2):1516–1523.

Zhang, Q. and Li, H. (2007). MOEA/D: A multiobjective evolutionary algorithm based on decomposition. *IEEE Transactions on Evolutionary Computation*, 11(6):712–731.